LAWRENCE
LIVERMORE
NATIONAL
LABORATORY

LLNL-TR-829538

# Seismo-Acoustic Wave Simulation for Earthquake-Generated Infrasound

K. Kim

November 30, 2021

## Disclaimer



This work performed under the auspices of the U.S. Department of Energy by Lawrence Livermore National Laboratory under Contract DE-AC52-07NA27344.

# Seismo-Acoustic Wave Simulation for Earthquake-Generated Infrasound

**Keehoon Kim**

Lawrence Livermore National Laboratory, Livermore, California, USA.

## Abstract

It is well known that underground explosions or earthquakes can generate infrasound in the atmosphere. Seismoacoustic coupling between the ground motions and atmosphere is a key mechanism for infrasound generation. Epicentral infrasound which is direct response to epicentral ground motions are extensively studied for event detection and discrimination. Diffracted infrasound generated from Rayleigh waves are often observed and reported. Recent studies suggested the surface topography is also important for infrasound generation, and mountains or topographic peaks can act as effective secondary infrasound sources. In this study, we perform full 3-D seismoacoustic simulations to understand a coupled seismic and acoustic wave generation by an earthquake and energy partitioning across the solid Earth-ocean-atmosphere system. By including the effects of realistic topography, bathymetry, and earthquake focal mechanism, we provide quantitative information about seismoacoustic wavefields and secondary infrasound sources across the solid-water, solid-air, and water-air interfaces. Acoustic wave transmission across water-air interface is also investigated by using synthetic waveforms. Our study suggests that shallow seas near the coastline or over elevated seafloors can transmit significant amount of energy from acoustic waves in water and can be effective secondary infrasound sources.

# 1. Introduction

The Earth's surface is often assumed to be opaque to mechanical wave propagation due to its high reflection coefficients. However, a growing number of observations indicate that the Earth's surface can allow for significant amount of energy transmission, which is important for seismoacoustic signal detection and source location for various geophysical phenomena [*Arrowsmith et al.*, 2010; *Marchetti et al.*, 2016; *Shani-Kadmiel et al.*, 2018; *Assink et al.*, 2018]. For the solid Earth-atmosphere boundary, the ground motions generated by underground explosions and earthquakes are effective secondary sources of acoustic waves in the atmosphere. Epicentral infrasound and diffracted infrasound along the surface have been identified and studied for event location and the estimation for the size of event [*Le Pichon et al.*, 2002; *Ford et al.*, 2014]. The ocean bottom also allows for coupling of seismic and acoustic waves in water generating tsunamis [*Maeda et al.*, 2013] and T-waves [*Wech et al.*, 2018]. The ocean-atmospheric boundary is generally not transparent for sound propagation due to their high contrast of acoustic impedances. However, recent theoretical studies suggest that they can be anomalously transparent for long-period sound waves with a shallow water depth [*Godin*, 2008a,b].

On 16 April 2016, a series of earthquakes with a $M_w$ 7.0 mainshock struck Kumamoto Prefecture in the central Kyushu of Japan. The Kumamoto earthquake sequence caused severe damage in the region by generating large strong motions, surface ruptures, subsequent landslides [*Kubo et al.*, 2016]. The ground motions during the mainshock was also felt in wide areas of southwest Japan [*Asano and Iwata*, 2016]. On 12 September 2016, a moderate intraplate earthquake ($M_L$ 5.8) occurred in Gyeongju, South Korea [*Woo et al.*, 2019], and its ground motions were felt even in Seoul, a city more than 300 km to the northwest. The source mechanism and rupture history of those earthquakes were investigated by various seismic data including strong ground motion, teleseismic body waves, and long-period surface waves [*Miyazawa*, 2016; *Hao et al.*, 2017; *Kim et al.*, 2017; *Woo et al.*, 2019]. Beside the seismic observations, infrasound signals induced by the earthquakes were also observed in infrasound arrays in South Korea. Those infrasound arrays have been installed and operated by Korean Institute of Geoscience and Mineral Resources (KIGAM) and used for explosion monitoring and analysis of earthquake-generated ground motion [*Che et al.*, 2010, 2020, 2021]. The KIGAM arrays recorded both epicentral and diffracted infrasound generated by the earthquake ground motions [*Le Pichon et al.*, 2002], and their back-projection for source locations [*Che et al.*, 2020, 2021] showed possible secondary infrasound sources distributed near the epicenter and propagation paths of seismic surface waves. The geometric pattern

of secondary infrasound source distribution should be affected by the seismic source mechanisms, intervening topography/bathymetry and Earth-ocean-atmosphere boundaries in the propagation paths.

In this study, we perform full 3-D seismoacoustic simulations for the 2016 Kumamoto and Gyeongju earthquakes. Previous seismoacoustic modelings often assumed a simple geometry for topography and bathymetry (e.g., flat or symmetrical) in 2-D [*Jones et al.*, 2015; *Martire et al.*, 2018]. However, such an oversimplified assumption may not be valid for the complex environment surrounding the Kumamoto earthquake, leading to insufficient simulation results to evaluate seismoacoustic energy partitioning along the boundaries. In this study, we include full 3-D topography/bathymetry and solid Earth-ocean-atmosphere boundaries to account for the effects of complex geometry in seimoacoustic waves transmission. These physics-based numerical simulations can provide theoretical insights on infrasound generation mechanisms in heterogeneous media and can be used to interpret infrasound signals generated by earthquakes.

# 2. Method

This section describes numerical modeling techniques used for seismoacoustic wave propagation. We mainly use the Elasto-Acoustic code (ElAc) developed by Lawrence Livermore National Laboratory (LLNL) [*Petersson and Sjögreen*, 2018] to simulate the coupling of earthquake generated ground motions to atmosphere and ocean water column. However, high-order finite-difference scheme used in ElAc does not allow for a sharp material contrast between water and solid and needs an additional numerical code to solve the problem. We use the infraFDTD code developed by *Kim et al.* [2014] particularly for acoustic coupling at ocean-atmosphere boundary. First, seismoacoustic simulations are run by ElAc to calculate ground motions and pressures on the ground, and then, the acoustic pressures calculated by ElAc are used as input for infraFDTD to simulate acoustic wave generation in the sea water columns and transmission through the water-atmosphere boundary. Full waveform simulations with heterogeneous media and complex boundary geometries are computationally expensive. We use High Performance Computing (HPC) resources in LLNL to cover large computation domain including the southwest of Japan and the east coast of South Korea.

## 2.1. ElAc code

*ElAc* is a full 3-D waveform simulation code for coupled seismic and acoustic wave propagation in the solid Earth and atmosphere. ElAc uses high-order finite difference method in time domain to solve the seismic wave equation in solid medium and the linearized Euler equations in moving atmospheres [*Petersson and Sjögreen*, 2018]. A fourth-order finite difference scheme based on the summation-by-part principle [*Strand*, 1994] is used to approximate seismic wave equation and sixth-order finite difference is used for acoustic waves. Seismo-acoustic coupling at the Earth's surface was achieved by imposing continuous boundary condition for normal particle velocities and normal stresses across the surface. The coupling of seismic and acoustic motion is often governed by complex topography of Earth's surface. ElAc allows for non-planar surface topography for simulation by using topography-following curvilinear coordinates.

*ElAc* solves the linearized Euler equations for an ideal and perfect gas. It can be applied to acoustic propagation in the atmospheres but may not be applicable to other fluids which are not described by the ideal gas law. We adapt the governing equation of *ElAc* in order to be applicable to sea water or other fluids for sound propagation. The linearized Euler equation of *ElAc* can be written for small perturbation of density ($\rho$), pressure ($p$), and particle velocity ($\mathbf{u}$) as follows [*Petersson and Sjögreen*, 2018].

$$\frac{\partial \rho}{\partial t} + (\hat{\mathbf{u}} \cdot \nabla)\rho + (\mathbf{u} \cdot \nabla)\hat{\rho} + \hat{\rho}\nabla \cdot \mathbf{u} + \rho \nabla \cdot \hat{\mathbf{u}} = f_p, \tag{1}$$

$$\frac{\partial \mathbf{u}}{\partial t} + (\hat{\mathbf{u}} \cdot \nabla)\mathbf{u} + (\mathbf{u} \cdot \nabla)\hat{\mathbf{u}} + \frac{1}{\hat{\rho}}\nabla p - \frac{\rho}{\hat{\rho}^2}\nabla \hat{p} = \mathbf{f}_\mathbf{u}, \tag{2}$$

$$\frac{\partial p}{\partial t} + (\hat{\mathbf{u}} \cdot \nabla)p + (\mathbf{u} \cdot \nabla)\hat{p} + \hat{\rho}\hat{c}^2 \nabla \cdot \mathbf{u} + \gamma p \nabla \cdot \hat{\mathbf{u}} = f_p, \tag{3}$$

where $\hat{\rho}$, $\hat{p}$, $\hat{\mathbf{u}}$, and $\hat{c}$ are material density, pressure, moving velocity (e.g., wind), and the speed of sound, respectively. In atmospheric acoustics, the terms $\nabla \cdot \hat{\mathbf{u}}$ and $\nabla \hat{p}$ can be small enough to be ignored [*Ostashev et al.*, 2005], and Equations (1) – (3) can be simplified as follows.

$$\frac{\partial \mathbf{u}}{\partial t} + (\hat{\mathbf{u}} \cdot \nabla)\mathbf{u} + (\mathbf{u} \cdot \nabla)\hat{\mathbf{u}} + \frac{1}{\hat{\rho}}\nabla p = \mathbf{f}_{\mathbf{u}}, \tag{4}$$

$$\frac{\partial p}{\partial t} + (\hat{\mathbf{u}} \cdot \nabla)p + \hat{\rho}\hat{c}^2 \nabla \cdot \mathbf{u} = f_p. \tag{5}$$

Note that Equations (4) and (5) were also derived by [*Ostashev et al.*, 2005] (Equations 17 and 18 in the reference) for sound propagation in arbitrary fluids. Hence, Equations (4) and (5) can be used for any fluid without the limitation of an ideal gas.

### 2.2. *infraFDTD code*

*infraFDTD* is a 3-D acoustic simulation code using a set of first-order, velocity-pressure-coupled differential equations to solve acoustic wave propagation in fluids [*Ostashev et al.*, 2005]. *infraFDTD* uses the staggered finite-difference time-domain (FDTD) algorithm [*Yee*, 1966] to approximate the derivatives in the wave equation. Time marching for the time-domain solution was also staggered between the computations of pressure and particle velocity. In the traditional CPU-based FDTD algorithm, the pressure and particle velocity at each node on each time step were updated by a sequential arithmetic operation taking up most of the CPU time. This time-consuming sequential operation was, however, replaced with parallel operations performed by many-core GPUs reducing the enormous amount of computation time [*Micikevicius*, 2009; *Lopez et al.*, 2013]. The perfectly matched layer technique [*Berenger*, 1994] was adopted for absorbing boundary conditions achieving highly effective suppression of reflections at the computational domain boundaries.

## 3. Simulation setup

### 3.1. *Solid Earth-Atmosphere and Solid Earth-Ocean Interface*

We use the modified ElAc to simulate wave propagation through the Solid Earth-Atmosphere and Solid Earth-Ocean interfaces. The modified governing equations in Equation (4) – (5) allows ElAc to treat seismoacoustic coupling between solid and arbitrary fluids including air and water. Figure 1 and 2 show geographical maps for numerical modeling. ElAc runs for regional seismoacoustic wave propagation for the larger rectangular area which extends $\sim$ 500 km in the north-south direction including the earthquake epicenter and the East Sea

Table 1: Simulation configuration

| | | CASE 1 | CASE 2 | CASE 3 |
|---|---|---|---|---|
| Method | | ElAc | ElAc | infraFDTD |
| Media interface | | Solid-Air | Solid-Water | Water-Air |
| Medium (Top) | Vp | 340 m/s | 1500 m/s | 340 m/s |
| | Density | 1.18 kg/m$^3$ | 1023 kg/m$^3$ | 1.18 kg/m$^3$ |
| Medium (Bottom) | Vp | 5670 m/s | 5670 m/s | 1500 m/s |
| | Vs | 3274 m/s | 3274 m/s | · |
| | Density | 2584 kg/m$^3$ | 2584 kg/m$^3$ | 1023 kg/m$^3$ |

of Korea. Although ElAc can be used for the interfaces between fluids and solid, it cannot be used for the Ocean and atmosphere boundary. This fluid-fluid boundary is treated as an internal boundary by ElAc unlike the solid-fluid boundary which is explicitly posed by the continuation condition of the stress and particle velocity [*Petersson and Sjögreen*, 2018]. The high-order finite difference scheme used in ElAc is not stable for a large contrast of material properties between air and water unless the codes are significantly modified to handle the boundary [*Haney*, 2007]. Hence, in this study, we assume two extreme cases for regional simulations (Table 1). For Case 1, the material above the solid Earth is assumed as air. This assumption can be valid when the seismoacoustic wave propagation is most governed by the solid Earth and atmosphere interface. For Case 2, the medium above the solid Earth is assumed as water. In this case, seismoacoustic waves are mostly governed by the solid Earth and ocean boundary in the simulation. These two simulations with completely different fluids can help us to understand how the water and air affects seismoacoustic wave coupling.

We use the USGS moment tensor solution of the Kumamoto ( available at https: //earthquake.usgs.gov/earthquakes /eventpage/us20005iis/executive, last access Sept. 1, 2021) and Gyeongju earthquakes (https://earthquake.usgs.gov/earthquakes/eventpage/us10006p1f/ executive) for the source mechanisms of ElAc simulation (Table 2). The source depth is 10 km from the surface for the Kumamoto earthquake and 13 km for the Gyeongju earthquake, and the source time functions ware assumed as a gaussian-type function with a corner frequency at 0.36 Hz. The global bathymetry and topography model at 15 arc second [*Tozer et al.*, 2019] is used to specify the elevation of the surface and ocean bottom in full 3-D. ElAc's computation domain is defined in 3-D curvilinear grid following the surface relief. The seismic and acoustic media are assumed homogeneous without internal stratification or structures [*Chang and Baag*, 2006].

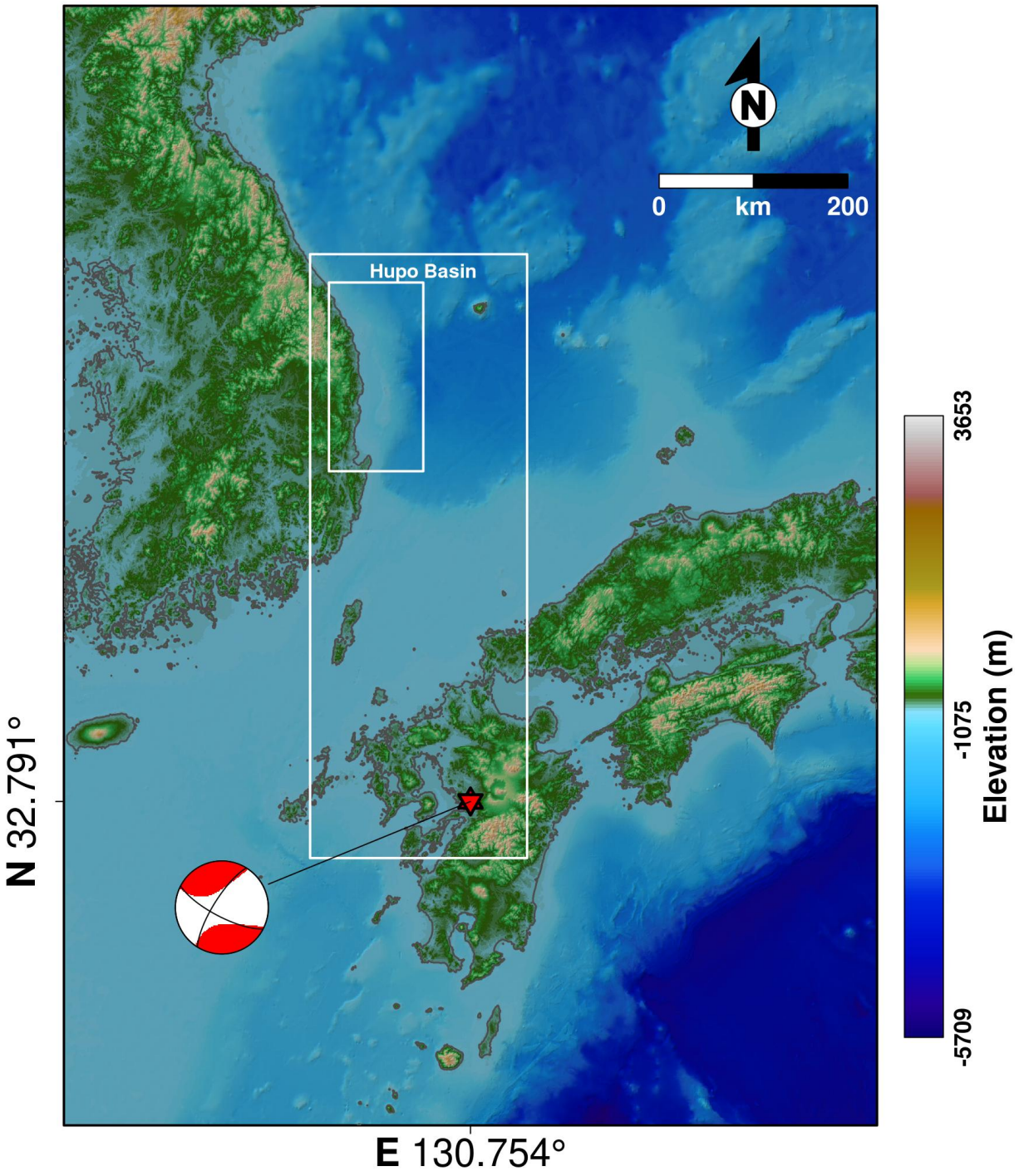


Figure 1: Geographical map for the 2016 Kumamoto earthquake. The epicenter of the earthquake (red star) and its focal mechanism are denoted.

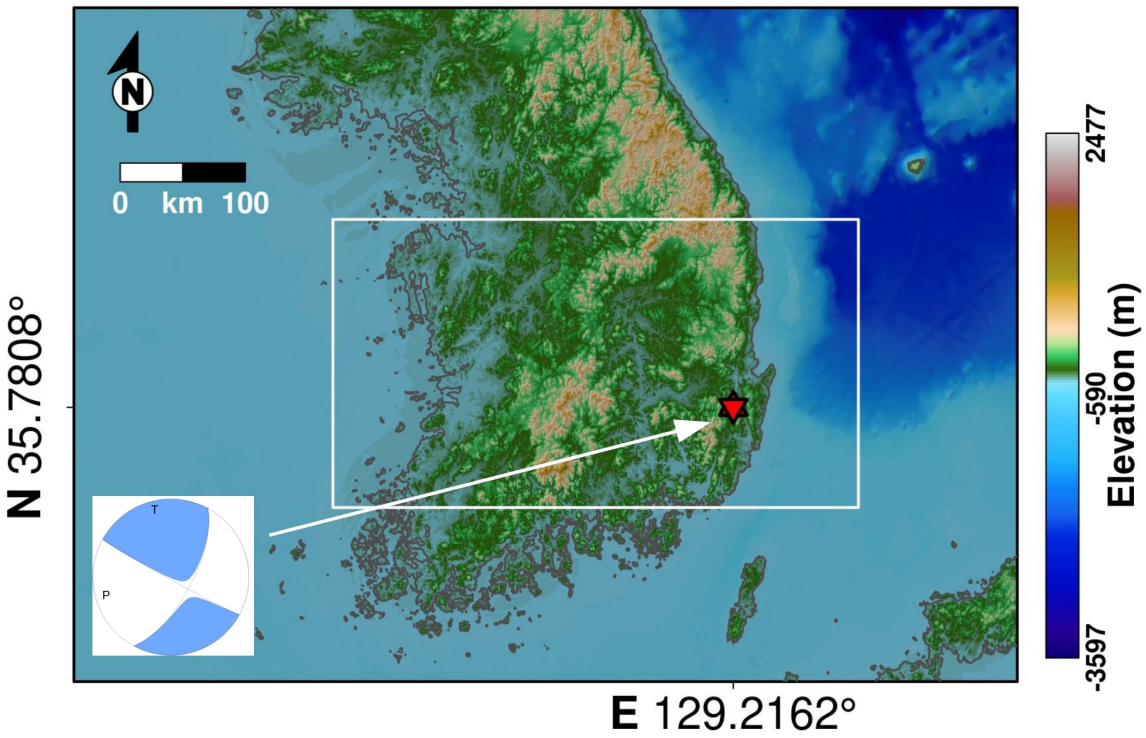


Figure 2: Geographical map for the 2016 Gyeongju earthquake. The epicenter of the earthquake (red star) and its focal mechanism are denoted.

Table 2: Moment tensor solution for the 2016 Kumamoto earthquake

| Event | $\mathbf{M_{xx}} \times 10^{16}$ (Nm) | $\mathbf{M_{yy}} \times 10^{16}$ (Nm) | $\mathbf{M_{zz}} \times 10^{16}$ (Nm) | $\mathbf{M_{xy}} \times 10^{16}$ (Nm) | $\mathbf{M_{xz}} \times 10^{16}$ (Nm) | $\mathbf{M_{yz}} \times 10^{16}$ (Nm) |
|---|---|---|---|---|---|---|
| Kumamoto | 4536 | -2922 | -1613 | -912 | -148 | -2226 |
| Gyeongju | 14.45 | 14.63 | 0.18 | -9.41 | 6.55 | -2.52 |

### 3.2. *Ocean-Atmosphere Interface*

Although ElAc using a high-order finite-difference is generally unstable for internal discontinuities, infraFDTD with a second-order accurate finite-difference time-domain (FDTD) method is more stable for a sharp contrast between material properties. InfraFDTD uses a staggered grid in space defining a pressure variable and material properties out of the discontinuity [*Ostashev et al.*, 2005]. With an arithmetic average of material velocity and density on the discontinuous air-water boundary, infraFDTD can treat acoustic wave propagation properly through the boundary [*Haney*, 2007]. In this study, we use the infraFDTD code to calculate acoustic transmission coefficient $T(z(x,y))$ on the water-air boundary. This simulation setup is denoted by Case 3 in Table 1. Unlike the prediction by classical ray theory, the transmission coefficient of incident waves on the water-air boundary can be affected by the water depth and wavelength [*Godin*, 2008a,b]. Hence, the full wave theory must be accounted for to calculate the transmission coefficient accurately. With the transmission coefficient $T(z(x,y))$ and the incident acoustic pressures $P_w(x,y)$ in water, we can approximate acoustic pressures $P_a(x,y)$ transmitted across the water-air interface as follows:

$$P_a(x,y) = T(z(x,y))P_w(x,y), \tag{6}$$

where $z(x,y)$ is a water depth at $x$ and $y$. It is assumed that the pressures on the ocean floor spherically radiate and attenuate by the geometrical spreading. A gaussian-type function with a corner frequency of 0.3 Hz is used as a point source to simulate spherical wave propagation in the water. We calculate an incident wavefield ($p_i$) in unbounded water without the presence of air and transmitted wavefield ($p_t$) at the water-air boundary with different water depths. The transmission coefficient $T(z(x,y))$ is computed by the ratio between them:

$$T(z(x,y)) = \frac{p_t(x,y)}{p_i(x,y)}. \tag{7}$$

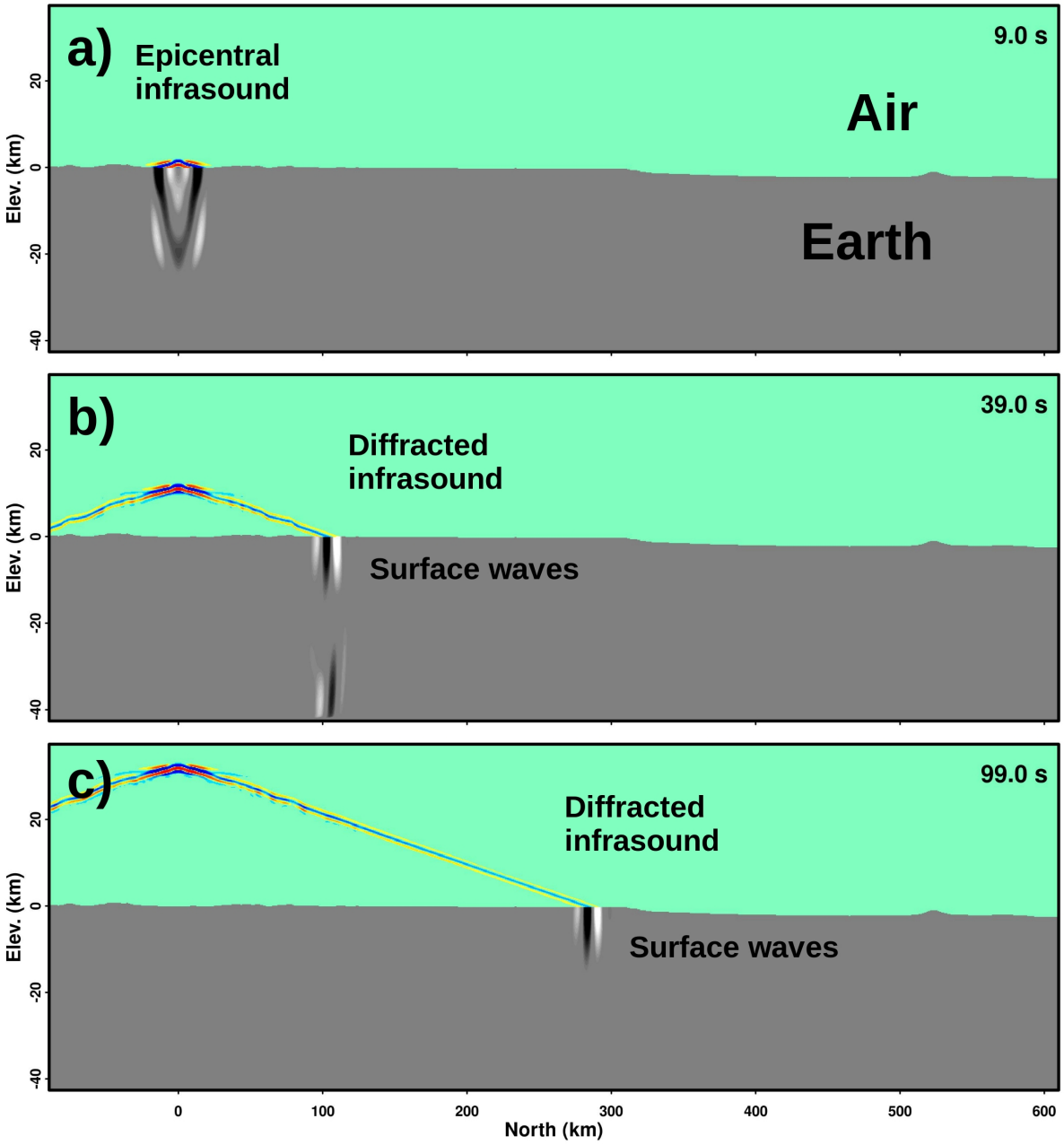


Figure 3: ElAc simulation for Case 1. Seismoacoustic wave propagation between solid Earth and atmosphere were simulated including topography and bathymetry. Propagating wavefields are captured in a vertical cross-section in the north-south direction. a) After the earthquake occurs, local seismic wave generation is dominated by a earthquake source mechanism. By the strong ground motion on the top of the hypocenter, epicentral infrasound is excited. b) and c) High-amplitude surface waves generate the diffracted infrasound which are often observed in regional distances.

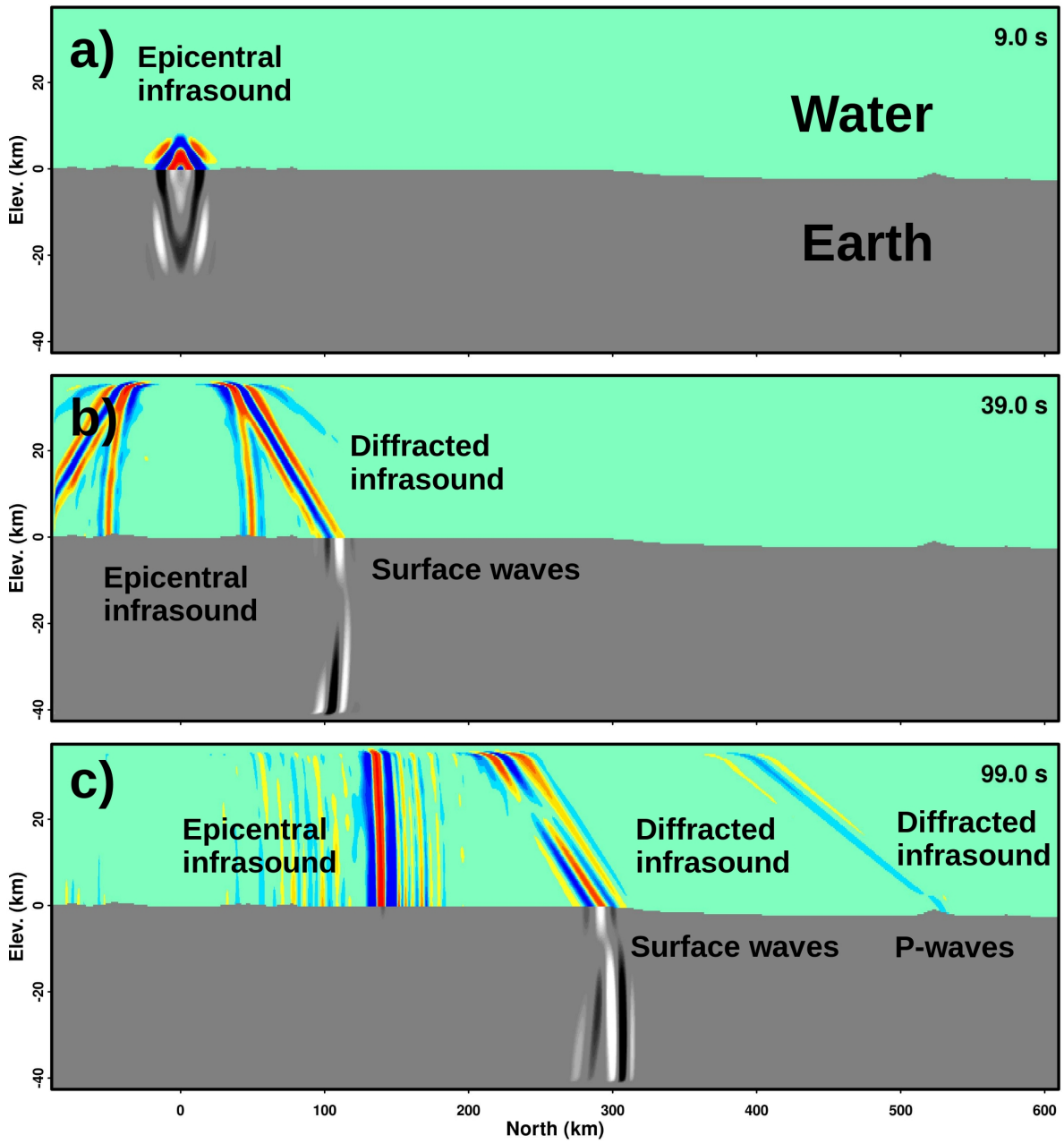


Figure 4: ElAc simulation for Case 2 including solid Earth and ocean interface. a) Like Case 1 for solid-air interface, early-stage seismoacoustic wavefields are characterized by epicentral infrasound in water and seismic body waves in the Earth. b) diffracted infrasound is excited by surface waves between the ground and water. c) Unlike the solid-air interface, epicentral infrasound in water is strong and expected to be dominant in regional distances in comparison with diffracted phases from seismic surface and body waves.

# 4. Results

## *4.1. Kumamoto Earthquake*

### 4.1.1. Case 1 and 2

We performed ElAc simulations for Case 1 and Case 2 for solid-air and solid-water interfaces (Table 1), respectively. Case 1 and 2 have the same source mechanism, topography, and bathymetry for simulations, but the medium above the ground is air for Case 1 and water for Case 2. Since the hypocenter of the Kumamoto and Gyeongju earthquake sits in the continental crust, Case 1 can represent seismoacoustic wave excitation and propagation in local distances near the epicenter. On the other hand, seismoacoustic waves observed near the Hupo Basin in the East Sea (Figure 1) can be explained by the Case 2 simulation due to their propagation path along solid-water interface.

Figure 3 and 4 show simulation results of Case 1 and 2 for the 2016 Kumamoto earthquake. The seismoacoustic wave images in Figure 3 and 4 were recorded in the north-south cross-section including the earthquake hypocenter. For both Case 1 and Case 2, seismoacoustic wavefield in local distances appeared to be governed by the source mechanism. Epicentral infrasound due to strong ground motion above the source are observed in the both cases (Figure 3a and 4a). For Case 1, strong seismic surface waves are developed at the ground-air interface as they propagate and result in diffracted infrasound (Figure 3b and 3c). Case 2 also shows diffracted infrasound in water due to surface waves traveling along the seafloor, but the epicentral infrasound in water appeared stronger than diffracted infrasound in regional distances (Figure 4b and 4c) in contrast to Case 1. This indicates that the seismic energy is more efficiently coupled into water than in air due to less acoustic impedance contrast, leading to strong epicentral infrasound in water. This epicentral acoustic waves will contribute to generating T-waves traveling in water if the hypocenter is placed below the ocean [*Wech et al.*, 2018].

Figure 5a) and 5b) show peak pressure amplitudes of infrasound recorded on the ground for Case 1 and Case 2, respectively. We only measured acoustic signals generated by local ground coupling except for epicentral infrasound. Relative amplitudes (dB) are obtained with respect to their maximum amplitudes near the epicenter. Infrasound radiation patterns near the epicenter are governed by the earthquake focal mechanism for both Case 1 and 2. The infrasound amplitude patterns are in good agreement with the Rayleigh wave radiation pattern for the given source mechanisms. This indicates that the diffracted infrasound are

direct response to the ground motion of Rayleigh waves [*Che et al.*, 2021]. While infrasound radiation patterns are similar in both air and water medium, relative amplitude attenuations are notably different. Peak amplitudes in water attenuate much faster than those in air. As the diffracted infrasound is directly affected by the ground motion of Rayleigh waves, this indicates that the Rayleigh wave amplitudes attenuate faster in water than in air. This different amplitude attenuation is confirmed by the synthetic acoustic waveforms for Case 1 and 2 in Figure 6. The acoustic waveforms are measured on the ground from the epicenter to the north, and their amplitudes are normalized with respect to the Rayleigh waves. Both cases recorded direct P-waves, Rayleigh waves (at the ground-air and ground-water interfaces), and epicentral acoustic waves. While the Rayleigh waves recorded at the ground-air interface (Figure 6a) continue to be dominant phases in the regional distances, the Rayleigh wave amplitudes at the ground-water interface (Figure 6b) attenuate quickly and become comparable to the P-wave amplitudes after long propagation distance. This is because those Rayleigh waves continuously lose their energy into the water due to less impedance contrast between the ground and water. However, the impedance difference between ground and air is much larger, and the seismic energy is well contained within the solid medium for Case 1. Leaking Rayleigh waves are often reported for the crust-mantle interface [*Hong et al.*, 2008], but similar energy loss is also expected for the ground-ocean interface based on this simulation.

#### 4.1.1. Case 3

For Case 3, we perform finite-difference simulations in 3-D with the infraFDTD code. Although the ElAc simulations for Case 1 and 2 provides quantitative information about energy transmission through the solid-air and solid-water interfaces, ElAc cannot be used for acoustic wave propagation between water and air due to their large contrast in acoustic impedance. Unlike ElAc using a higher-order finite difference scheme, infraFDTD uses a second-order finite difference scheme which can be applied to a medium with high material contrast.

Figure 7 shows acoustic wave propagation through the air-water interface. Two cases with different water depths are simulated to address the effects of source depth in water. Both cases include two layers of water and air, and a point source with a cut-off frequency at 0.3 Hz is placed on the ground in the water layer. Figure 7a and 7b show the images of wave propagation at a water depth of 5 km which is comparable to the simulated wavelength (5 km at 0.3 Hz). When upward traveling waves strike the water-air interface, most of energy is reflected back to the water due to high contrast in acoustic impedance between water and

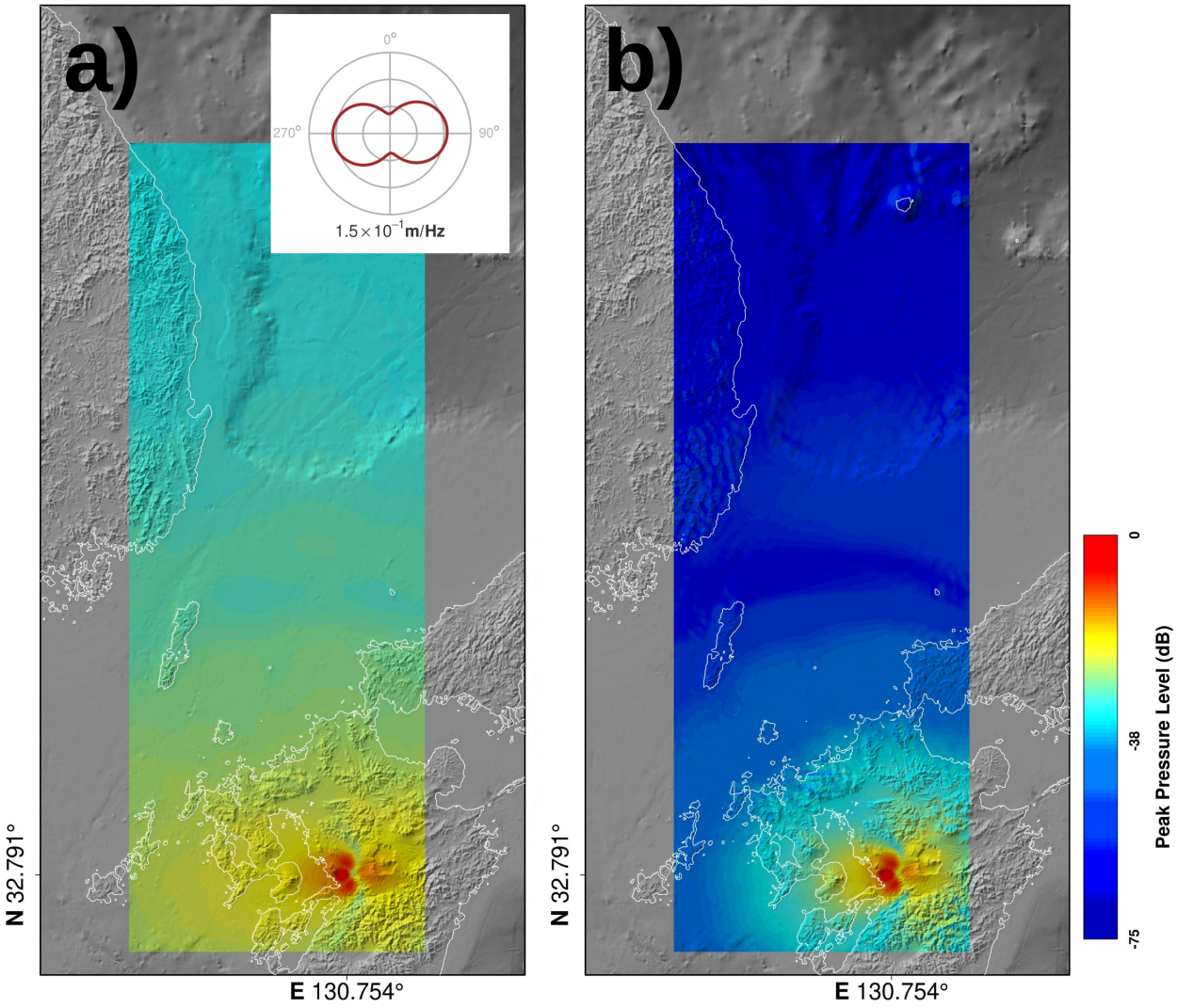


Figure 5: Peak pressure amplitudes (dB) recorded on the ground surface for Case 1 (a) and 2 (b). Amplitudes are measured only for locally coupled infrasound except for epicentral infrasound, and their relative amplitudes are plotted with respect to the maximum amplitudes near the epicenter. Theoretical radiation pattern of Rayleigh waves for the given focal mechanism is also denoted on the top of a).

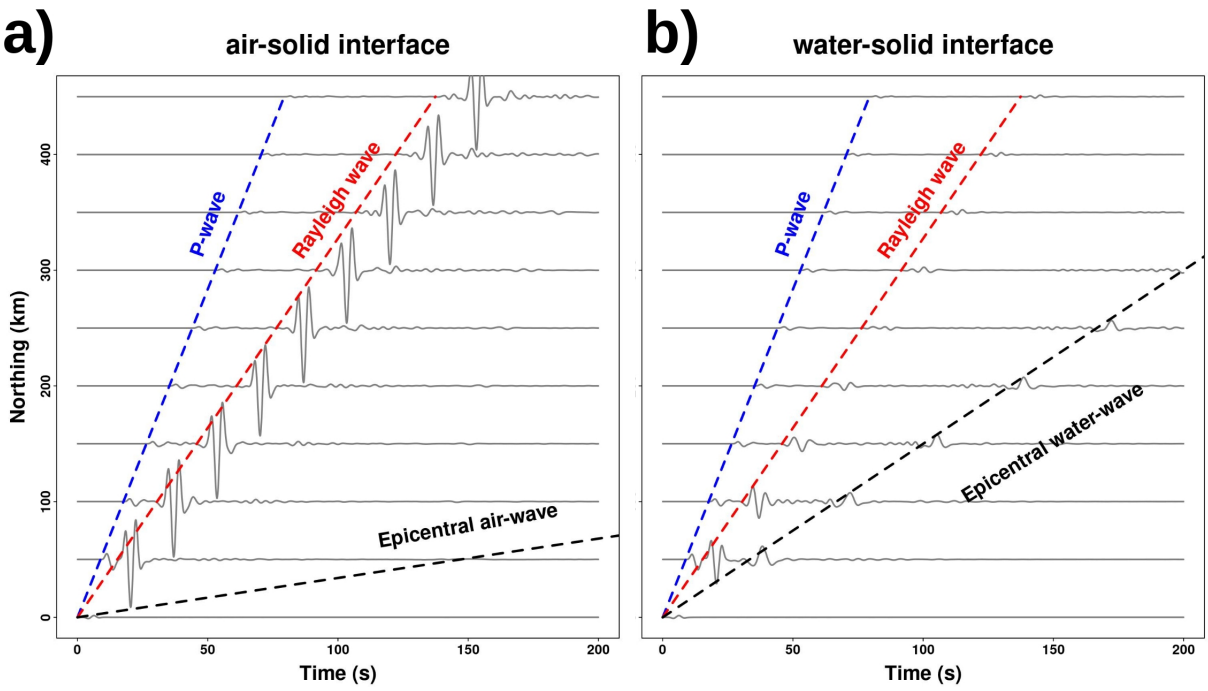


Figure 6: Synthetic acoustic waveforms recorded on the ground for Case 1 (a) and Case 2 (b). The acoustic pressures were measured from the epicenter to the north and normalized with respect to the peak amplitudes of Rayleigh waves.

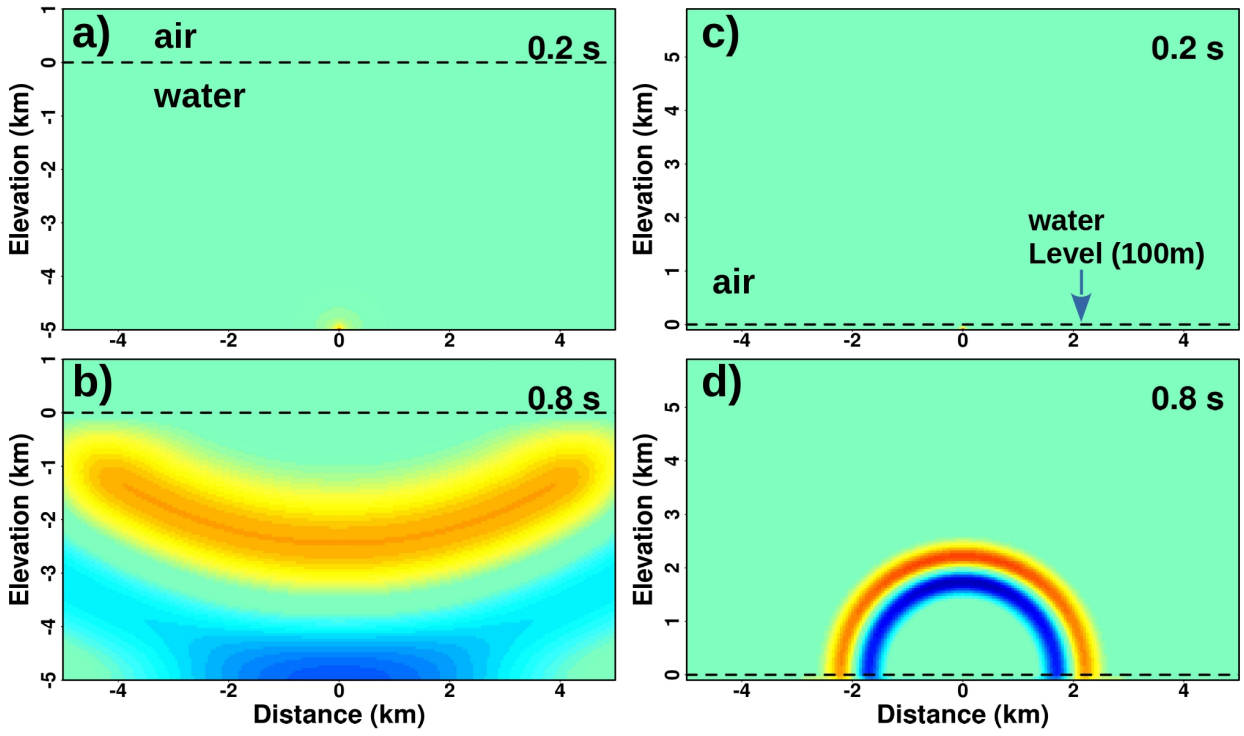


Figure 7: Acoustic wave propagation simulations for Case 3 using infraFDTD. The simulation medium consists of two layers: the air layer on the top of water. A point source is placed on the ground in the water layer. Two different water depths are simulated: 5 km for a) - b) and 100 m for c) - d). If the water depth is comparable to the wavelength (5 km at 0.3 Hz), incident waves are reflected from the water-air interface due to large acoustic impedance contrast (b). However, if the water depth is a fraction of wavelength, significant acoustic energy is transmitted into air through the interface d).

air. One the other hand, Figure 7c and 7d with a water depth of 100 m show different results. Incident waves in Figure 7d transmit significant energy into air, creating spherically wave propagation in air. This indicates the water-air interface can be anomalously transparent for acoustic wave transmission when the water depth is a fraction of wavelength. This anomalous transparency can be created by the contribution of inhomogeneous (evanescent) waves at the interface. In general, evanescent waves cannot generate net time-averaged power, but the interference of incident and reflected evanescent waves in shallow water allows for transmitting a non-zero time-averaged power [*Godin*, 2008a; *Calvo et al.*, 2013].

We verify the infraFDTD simulation results with a theoretical solution. The pressure field radiated from a monopole in unbounded water can be written as

$$p_i = p_0 R_0 \frac{e^{ik_w R}}{R}, \tag{8}$$

where $R = \sqrt{x^2 + y^2 + z^2}$ and $k_w = 2\pi f / c_w$. A frequency of wave and the sound speed of water are denoted by $f$ and $c_w$, respectively. $p_0$ is the pressure measured at distance $R_0$. When the propagating pressures pass the water-air interface, the total wavefield can be decomposed into the incident and reflected waves in water and transmitted waves in air. The transmitted pressure can be expressed by wavenumber integration [*Calvo et al.*, 2013] as follows.

$$p_t = i p_0 R_0 \int_0^\infty \frac{q}{s_w} J_0(qr)[W(q) e^{i s_w D} e^{i s_a z}] dq, \tag{9}$$

$$r = \sqrt{x^2 + y^2}, s_w = \sqrt{k_w^2 - q^2}, s_a = \sqrt{k_a^2 - q^2}, \tag{10}$$

$$W = \frac{2 m s_w}{s_a + m s_w}, m = \frac{\rho_a}{\rho_w}, n = \frac{c_w}{c_a}, \tag{11}$$

where $D$ is the source depth, $k_a = 2\pi f / c_a$, and $c_a$ is the sound speed of air. We solved this wavenumber integration by the trapezoidal rule [*Jensen et al.*, 2011]. Transmission coefficients ($p_t / p_i$) in Equation 7 are calculated on the vertical axis ($r = 0$) at the interface and compared with the infraFDTD results. Figure 8 shows transmission coefficients calculated at 0.3 Hz by the wavenumber integration and infraFDTD with respect to different depths. The transmission coefficients increase dramatically as the source depth in water decreases, and the results of two methods are in good agreement. There are small differences between two results which might be caused by numerical accuracy and boundary condition of infraFDTD. Unlike the wavenumber integration theoretically defined in unbounded space,

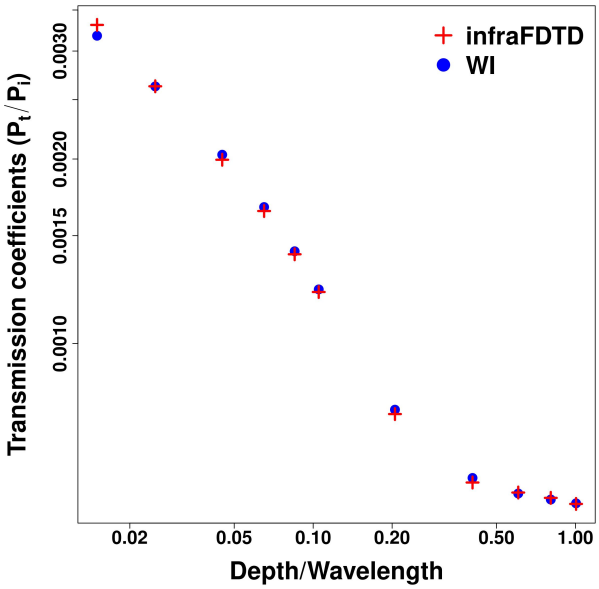


Figure 8: Transmission coefficients (Equation 7) calculated by infraFDTD (red cross) and the wavenumber integration (blue circle).

infraFDTD runs on truncated computation domain surrounded by absorbing layers. This absorbing layers suppress wave reflection on the computation domain effectively, but small amplitudes of reflected waves can still exist, affecting the transmission coefficient calculation.

We finally predict infrasound amplitudes on the water surface over Hupo Basin. Figure 9 shows the incident acoustic pressures at the water level (a), transmission coefficients (b), and transmitted pressures in air (c). The incident acoustic pressures are calculated from the ElAc simulation for Case 2. As the seismoacoustic waves in Hupo Basin propagated from the source through the ground-water interfaces, Case 2 with a water layer should be more appropriate for acoustic pressure prediction over Hupo Basin. During the Case 2 simulation, acoustic pressures are recorded at water surface levels, and peak pressure amplitudes are measured (Figure 9a). Transmission coefficients over Hupo Basin (Figure 9b) are calculated based on Figure 8 and bathymetry. Finally, peak acoustic pressures on the water surface in air (Figure 9c) are predicted by multiplying the incident waves by the transmission coefficients. The peak pressures of incident waves in unbounded water are generally governed by the distance from the source and roughness of seafloor, showing high amplitudes in the south. The transmission coefficients strongly depend on the water depth and have large values along the coastline. The resultant transmitted pressures in air shows combined effects. Due to high transmission coefficients, acoustic pressures on the water surface are generally large in

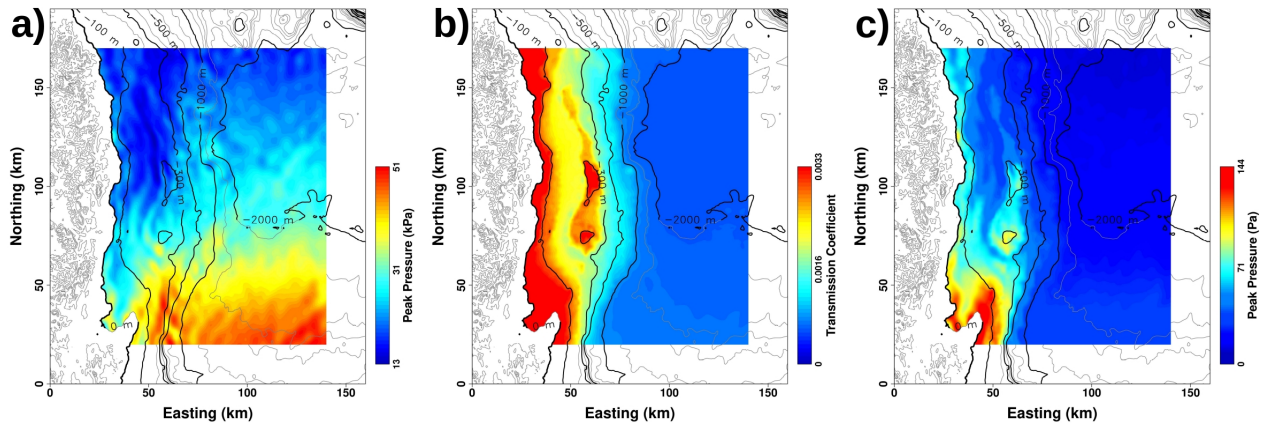


Figure 9: a) Peak pressure amplitudes in water over Hupo Basin, calculated by ElAc for Case 2. b) Transmission coefficients depending on water depths. c) Peak pressures of transmitted acoustic waves on the water surface in air.

the shallow water along the coastline and largest in the southern coastline. High acoustic pressures in air are also predicted along the edge of Hupo Basin due to its high elevation. This simulation results can be used to locate possible secondary infrasound sources. Infrasound amplitudes are generally governed by radiation patterns due to source mechanisms. It is also reported that surface topography can amply infrasound amplitudes by focusing seismic energy [*Che et al.*, 2021]. However, our research indicates shallow water depths allow for anomalous transmission of acoustic waves across water-air interfaces and can contribute to secondary infrasound sources in the atmosphere.

## *4.2. Gyeongju Earthquake*

### 4.2.2. Case 1 and 2

Simulation results for the Gyeongju earthquake are shown in Figure 10. Figure 10a) and 10b) plot peak pressure amplitudes of acoustic waves recorded on the ground for Case 1 and Case 2, respectively. We only measured acoustic signals generated by local ground coupling except for epicentral infrasound. Relative amplitudes (dB) are calculated with respect to the maximum amplitudes of Case 2 (Figure 10b). Infrasound radiation patterns near the epicenter are governed by the earthquake focal mechanism for both Case 1 and 2 as shown in the Kumamoto earthquake simulations. While infrasound radiation patterns are similar in both air and water medium, their peak amplitudes are different for Case 1 and 2. Peak amplitudes in water show much larger than those in air. Although the ground motions

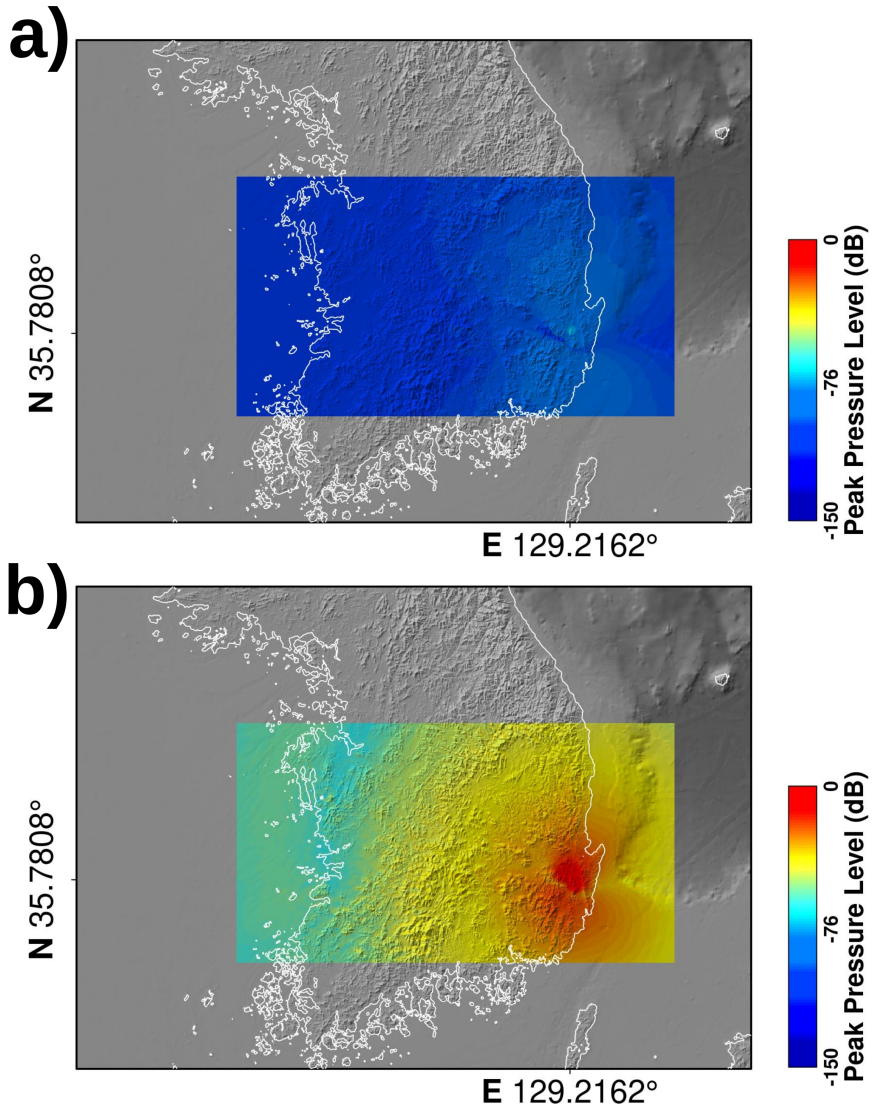


Figure 10: Peak pressure amplitude (dB) recorded on the ground surface for Case 1 (a) and 2 (b) for the 2016 Gyeongju earthquake. Amplitudes are measured only for locally coupled infrasound except for epicentral infrasound, and the peak pressures for both Case 1 and 2 are scaled with respect to the largest amplitudes in Case 2 (b).

of Rayleigh waves in the air-solid interface are much larger than those in the water-solid interface (as discussed in the Kumamoto earthquake simulations), converted pressures in the water are generally larger than the pressures in the air. This is because the acoustic impedance difference between ground and water is much smaller than the difference between ground and air, and the seismic energy associated with the Rayleigh waves can be efficiently transmitted into the water generating larger acoustic pressures.

#### 4.2.2. Case 3

Predicted infrasound amplitudes on the water surface are plotted in Figure 11. Figure 11 shows the incident acoustic pressures at the water level (a), transmission coefficients (b), and transmitted pressures in air (c). As the case of Kumamoto earthquake simulations, the incident acoustic pressures are calculated from the ElAc simulation for Case 2, and acoustic pressures are measured at water surface levels in the simulation (Figure 11a). Transmission coefficients across water-air interface (Figure 11b) are calculated based on Figure 8 and bathymetry, and peak acoustic pressures on the water surface in air (Figure 11c) are predicted by multiplying the incident waves by the transmission coefficients. The transmission coefficients strongly depend on the water depth and have large values along the coastline as the Kumamoto case shown in Figure 9b). Due to high transmission coefficients and large incident pressures near the epicenter, acoustic pressures on the water surface are generally large in the shallow water along the eastern coastline. Unlike the eastern coastline, low acoustic pressure levels are predicted on the water surface near the western coastline although the transmission coefficients along the western coastline are as large as the east coast. This is due to the small amplitudes of incident pressures in the West Sea, which is predicted by the ElAc simulation for Case 2. As the Rayleigh wave ground motions attenuate rapidly in the propagation along the solid-water interface, acoustic pressures induced by the Rayleigh motions are predicted significantly smaller than the pressures in the East Sea (Figure 11a). However, the acoustic pressures in the West Sea should be underestimated by the ElAc simulation (Case 2) assuming water-solid interface across the modeling domain. In the actual environment, the Rayleigh wave attenuation from the epicenter to the west coast is not as large as the prediction by Case 2 because the Rayleigh waves travel in the solid-air interface. In this case, the Rayleigh waves can propagate efficiently without significant loss of seismic energy, and the ground motions over the seafloor in the West Sea could be significantly larger than the prediction in Figure 11a.

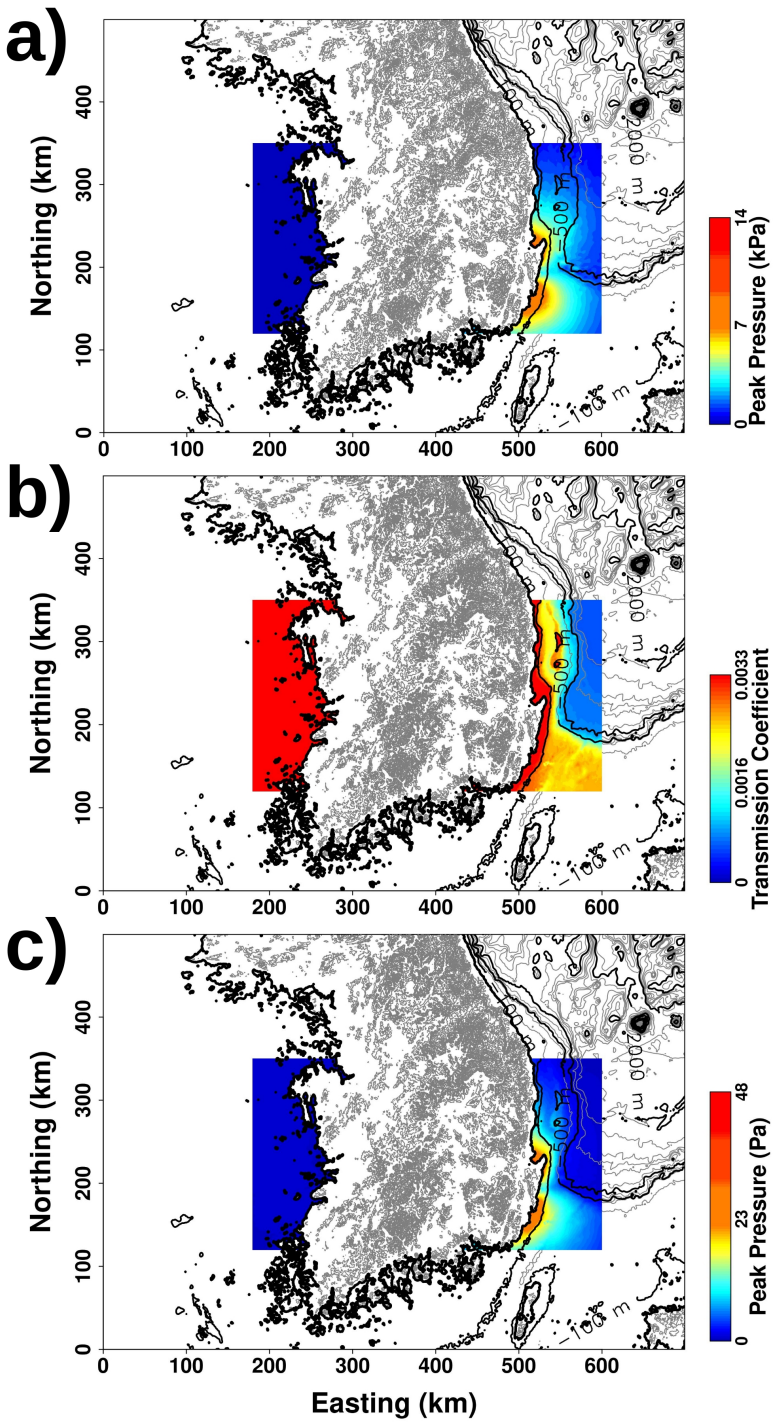


Figure 11: a) Peak pressure amplitudes in water, calculated by ElAc for Case 2. b) Transmission coefficients calculated by infraFDTD. c) Peak pressures of transmitted acoustic waves on the water surface in air.

# 5. Concluding remarks

We performed full 3-D seismoacoustic simulation for energy transmission across the solid Earth-atmosphere, solid Earh-ocean, and ocean-atmosphere boundaries. Complex topography, bathymetry, and seismic source mechanisms were included, providing quantitative prediction for seismoacoustic wave generation and propagation in realistic environment. The ElAc codes, high-order finite-difference solver, are used for seismoacoustic coupling between solid-water and solid-air interfaces. It was shown that the ground motions generated by Rayleigh waves were dominant sources of diffracted infrasound in air or water. However, diffracted infrasound attenuated faster in solid-water interface than solid-air interface due to the Rayleigh waves leaking their energy into water. The infraFDTD codes, second-order finite-difference solver, are used to calculate acoustic transmission coefficients between water and air. It showed that a water-air interface is generally opaque for acoustic wave propagation but can be anomalously transparent if the water depth is significantly shorter than the wavelength. These methods were applied for the 2016 Kumamoto earthquake and the 2016 Gyeongju earthquake to predict infrasound signals recorded on infrasound stations in South Korea. The results suggested that shallow seas near the coastline or over elevated seafloors can be effective secondary infrasound sources in the atmosphere.

## Acknowledgments

The ElAc code was developed with support from LLNL Laboratory Directed Research and Development project 14-ER-001. infraFDTD is developed by the author (Keehoon Kim) and an open source code available upon request. This work was performed under the auspices of the U.S. Department of Energy by Lawrence Livermore National Laboratory under Contract DE-AC52-07NA27344.

# References

Arrowsmith, S. J., J. B. Johnson, D. P. Drob, and M. A. H. Hedlin (2010), The seismoacoustic wavefield: A new paradigm in studying geophysical phenomena, *Rev. Geophys.*, *48*(4), RG4003.

Asano, K., and T. Iwata (2016), Source rupture processes of the foreshock and mainshock in the 2016 kumamoto earthquake sequence estimated from the kinematic waveform inversion

of strong motion data, *Earth, Planets and Space*, *68*(1), 147, doi:10.1186/s40623-016-0519-9.

Assink, J., G. Averbuch, S. ShaniKadmiel, P. Smets, and L. Evers (2018), A SeismoAcoustic Analysis of the 2017 North Korean Nuclear Test, *Seismological Research Letters*, *89*(6), 2025–2033, doi:10.1785/0220180137.

Berenger, J. (1994), A perfectly matched layer for the absorption of electromagnetic waves, *Journal of computational physics*, *114*(2), 185–200, doi:10.1006/jcph.1994.1159.

Calvo, D. C., M. Nicholas, and G. J. Orris (2013), Experimental verification of enhanced sound transmission from water to air at low frequencies, *The Journal of the Acoustical Society of America*, *134*(5), 3403–3408, doi:10.1121/1.4822478.

Chang, S.-J., and C.-E. Baag (2006), Crustal Structure in Southern Korea from Joint Analysis of Regional Broadband Waveforms and Travel Times, *Bulletin of the Seismological Society of America*, *96*(3), 856–870, doi:10.1785/0120040165.

Che, I.-Y., H.-I. Lee, J.-S. Jeon, I.-C. Shin, and H.-C. Chi (2010), State-of-the-art studies on infrasound monitoring in korea, *Geophysics and Geophysical Exploration*, *13*(3), 286–294.

Che, I.-Y., Y.-W. Yun, and I. S. Lim (2020), Analysis of ground-motion characteristics of the 2004 offshore uljin earthquake through atmospheric infrasound observation, *Journal of the Korean earth science society*, *41*(6), 647–657.

Che, I.-Y., K. Kim, A. LePichon, J. Park, S. Arrowsmith, and B. Stump (2021), Illuminating the North Korean nuclear explosion test in 2017 using remote infrasound observations, *Geophysical Journal International*, *228*(1), 308–315, doi:10.1093/gji/ggab338.

Ford, S. R., A. J. Rodgers, H. Xu, D. C. Templeton, P. Harben, W. Foxall, and R. E. Reinke (2014), Partitioning of seismoacoustic energy and estimation of yield and height-of-burst/depth-of-burial for near-surface explosions, *Bulletin of the Seismological Society of America*, *104*(2), 608–623, doi:10.1785/0120130130.

Godin, O. A. (2008a), Low-frequency sound transmission through a gasliquid interface, *The Journal of the Acoustical Society of America*, *123*(4), 1866–1879, doi:10.1121/1.2874631.

Godin, O. A. (2008b), Sound transmission through waterair interfaces: new insights into an old problem, *Contemporary Physics*, *49*(2), 105–123, doi:10.1080/00107510802090415.

Haney, M. M. (2007), Generalization of von neumann analysis for a model of two discrete half-spaces: The acoustic case, *GEOPHYSICS*, *72*(5), SM35–SM46, doi:10.1190/1.2750639.

Hao, J., C. Ji, and Z. Yao (2017), Slip history of the 2016 mw 7.0 kumamoto earthquake: Intraplate rupture in complex tectonic environment, *Geophysical Research Letters*, *44*(2), 743–750, doi:https://doi.org/10.1002/2016GL071543.

Hong, T.-K., C.-E. Baag, H. Choi, and D.-H. Sheen (2008), Regional seismic observations of the 9 october 2006 underground nuclear explosion in north korea and the influence of crustal structure on regional phases, *Journal of Geophysical Research: Solid Earth*, *113*(B3), doi:https://doi.org/10.1029/2007JB004950.

Jensen, F. B., W. A. Kuperman, M. B. Porter, H. Schmidt, and A. Tolstoy (2011), *Computational ocean acoustics*, vol. 2011, Springer.

Jones, K. R., R. W. Whitaker, and S. J. Arrowsmith (2015), Modelling infrasound signal generation from two underground explosions at the source physics experiment using the rayleigh integral, *Geophysical Journal International*, *200*(2), 777–788, doi:10.1093/gji/ggu433.

Kim, K., J. M. Lees, and M. C. Ruiz (2014), Source mechanism of vulcanian eruption at Tungurahua Volcano, Ecuador, derived from seismic moment tensor inversions, *Journal of Geophysical Research: Solid Earth*, *119*(2), 1145–1164, doi:10.1002/2013JB010590.

Kim, Y., X. He, S. Ni, H. Lim, and S. Park (2017), Earthquake Source Mechanism and Rupture Directivity of the 12 September 2016 Mw5.5 Gyeongju, South Korea, Earthquake, *Bulletin of the Seismological Society of America*, *107*(5), 2525–2531, doi:10.1785/0120170004.

Kubo, H., W. Suzuki, S. Aoi, and H. Sekiguchi (2016), Source rupture processes of the 2016 kumamoto, japan, earthquakes estimated from strong-motion waveforms, *Earth, Planets and Space*, *68*(1), 161, doi:10.1186/s40623-016-0536-8.

Le Pichon, A., J. Guilbert, A. Vega, M. Garcs, and N. Brachet (2002), Ground-coupled air waves and diffracted infrasound from the arequipa earthquake of june 23, 2001, *Geophysical Research Letters*, *29*(18), 33–1–33–4, doi:https://doi.org/10.1029/2002GL015052.

Lopez, J. J., D. Carnicero, N. Ferrando, and J. Escolano (2013), Parallelization of the finite-difference time-domain method for room acoustics modelling based

on CUDA, *Mathematical and Computer Modelling*, *57*(78), 1822 – 1831, doi: http://dx.doi.org/10.1016/j.mcm.2011.11.075.

Maeda, T., T. Furumura, S. Noguchi, S. Takemura, S. Sakai, M. Shinohara, K. Iwai, and S. Lee (2013), Seismic and TsunamiWave Propagation of the 2011 Off the Pacific Coast of Tohoku Earthquake as Inferred from the TsunamiCoupled FiniteDifference Simulation, *Bulletin of the Seismological Society of America*, *103*(2B), 1456–1472, doi: 10.1785/0120120118.

Marchetti, E., G. Lacanna, A. Le Pichon, D. Piccinini, and M. Ripepe (2016), Evidence of Large Infrasonic Radiation Induced by Earthquake Interaction with Alluvial Sediments, *Seismological Research Letters*, *87*(3), 678–684, doi:10.1785/0220150223.

Martire, L., et al. (2018), Numerical simulation of the atmospheric signature of artificial and natural seismic events, *Geophysical Research Letters*, *45*(21), 12,085–12,093, doi: https://doi.org/10.1029/2018GL080485.

Micikevicius, P. (2009), 3d finite difference computation on gpus using cuda, in *Proceedings of 2nd Workshop on General Purpose Processing on Graphics Processing Units*, GPGPU-2, pp. 79–84, ACM, New York, NY, USA, doi:10.1145/1513895.1513905.

Miyazawa, M. (2016), An investigation into the remote triggering of the oita earthquake by the 2016 mw 7.0 kumamoto earthquake using full wavefield simulation, *Earth, Planets and Space*, *68*(1), 205, doi:10.1186/s40623-016-0585-z.

Ostashev, V., D. Wilson, L. Liu, D. Aldridge, N. Symons, and D. Marlin (2005), Equations for finite-difference, time-domain simulation of sound propagation in moving inhomogeneous media and numerical implementation, *The Journal of the Acoustical Society of America*, *117*, 503, doi:10.1121/1.1841531.

Petersson, N. A., and B. Sjögreen (2018), High order accurate finite difference modeling of seismo-acoustic wave propagation in a moving atmosphere and a heterogeneous earth model coupled across a realistic topography, *Journal of Scientific Computing*, *74*(1), 290–323, doi:10.1007/s10915-017-0434-7.

Shani-Kadmiel, S., J. D. Assink, P. S. M. Smets, and L. G. Evers (2018), Seismoacoustic coupled signals from earthquakes in central italy: Epicentral and secondary sources of infrasound, *Geophysical Research Letters*, *45*(1), 427–435, doi: https://doi.org/10.1002/2017GL076125.

Strand, B. (1994), Summation by parts for finite difference approximations for d/dx, *Journal of Computational Physics*, *110*(1), 47 – 67, doi:http://dx.doi.org/10.1006/jcph.1994.1005.

Tozer, B., D. T. Sandwell, W. H. F. Smith, C. Olson, J. R. Beale, and P. Wessel (2019), Global bathymetry and topography at 15 arc sec: Srtm15+, *Earth and Space Science*, *6*(10), 1847–1864, doi:https://doi.org/10.1029/2019EA000658.

Wech, A., G. Tepp, J. Lyons, and M. Haney (2018), Using earthquakes, t waves, and infrasound to investigate the eruption of bogoslof volcano, alaska, *Geophysical Research Letters*, *45*(14), 6918–6925, doi:https://doi.org/10.1029/2018GL078457.

Woo, J.-U., J. Rhie, S. Kim, T.-S. Kang, K.-H. Kim, and Y. Kim (2019), The 2016 Gyeongju earthquake sequence revisited: aftershock interactions within a complex fault system, *Geophysical Journal International*, *217*(1), 58–74, doi:10.1093/gji/ggz009.

Yee, K. (1966), Numerical solution of initial boundary value problems involving maxwell's equations in isotropic media, *IEEE Transactions on antennas and propagation*, *14*(3), 302–307, doi:10.1109/TAP.1966.1138693.